



# Glacial and tidal strain of landfast sea ice in Terra Nova Bay, East Antarctica, observed by interferometric SAR techniques



Hyangsun Han<sup>a</sup>, Hoonyol Lee<sup>b,\*</sup>

<sup>a</sup> Unit of Arctic Sea-Ice Prediction, Korea Polar Research Institute, Incheon 21990, Republic of Korea

<sup>b</sup> Division of Geology and Geophysics, Kangwon National University, Chuncheon, Kangwon-do 24341, Republic of Korea

## ARTICLE INFO

### Keywords:

Fast ice  
Strain  
Campbell Glacier Tongue  
Terra Nova Bay  
COSMO-SkyMed  
InSAR  
DDInSAR

## ABSTRACT

The dynamics of landfast sea ice, also called fast ice for short, has a large influence on the variability of polynyas and marine ecosystems, and the logistics for research stations near the Antarctic coast. Therefore, it is important to accurately measure the strain of fast ice and its seasonal variations, and to identify the cause of stresses on the ice. In this paper, we separate the strains from glacial stress and tidal stress of fast ice near the Campbell Glacier Tongue (CGT) in Terra Nova Bay, East Antarctica. This was done using observations from a series of one-day tandem COSMO-SkyMed Interferometric Synthetic Aperture Radar (InSAR) images obtained from December 2010 to January 2012. Firstly, we discriminated fast ice from pack ice and open water by analyzing the interferometric coherence values. We then identified the characteristics of the strains by investigating the equi-displacement lines of fringes in weekly InSAR and double-differential InSAR (DDInSAR) images. The weekly InSAR images predominantly showed glacial shear strain of the fast ice with fringes parallel to the sides of the CGT. This was due to the cumulative flow of the CGT for a week, while oscillating tidal signals were relatively small. The DDInSAR images, which cancelled glacial strain rates in two one-day InSAR images, showed a deformation of the fast ice by tidal sea surface tilt, with the fringes parallel to the coastline. Based on the unique characteristics of these strains, we separated them from the one-day InSAR images by decomposing the fringe patterns into glacial and tidal strain. Glacial shear strain rates of fast ice attached to the east of the CGT decreased from May to August owing to ice thickening and then stabilized until December. Those to the west of the CGT increased from May to July. This was possibly due to bottom melting of the ice by the increased ocean circulation during the expansion period of the nearby polynya. The glacial strain then decreased until December because of reduced polynya activity. The fast ice near the Jang Bogo Station (JBS) only showed tidal strain as it was isolated from the CGT by cracks and leads. Tidal strain rates of the fast ice were strongly correlated with the magnitude of tidal variations in all these regions, which represents shows that the tidal strain represents tidal sea surface tilt. The tidal response of fast ice to the west of the CGT and near the JBS was stronger than that to the east of the CGT, probably owing to thinner ice thickness there.

## 1. Introduction

Landfast sea ice, often called fast ice for short, is a type of sea ice that is fastened to the coastline, ice shelves, or glacier tongues (Massom et al., 2001; Giles et al., 2008; Fraser et al., 2012; Kim et al., 2015). Unlike pack ice or drift ice, fast ice does not move owing to currents or winds. In the Antarctic Ocean, fast ice accounts for ~5% of total sea ice area (Nihashi and Ohshima, 2015). In spite of its tiny stake in the Antarctic sea ice area, fast ice significantly influences the variability in coastal polynyas, sea ice production, and marine ecosystems (Trevena et al., 2003; Nihashi and Ohshima, 2015). Therefore, the analysis of spatiotemporal variations of fast ice dynamics in the Antarctic Ocean is

very important to understand environmental changes in the region.

The Terra Nova Bay (TNB) in the eastern Ross Sea is one of the representative regions for fast ice formation in East Antarctica (Fraser et al., 2012; Han et al., 2015; Kim et al., 2015; Nihashi and Ohshima, 2015). In this region, fast ice forms around the Campbell Glacier Tongue (CGT), which is an ice tongue extending from the Campbell Glacier into the ocean. Two Antarctic research stations, Jang Bogo Station (JBS) operated by the Korea Polar Research Institute (KOPRI), and Mario Zucchelli Station (MZS), operated by the Italian Programma Nazionale di Ricerche in Antartide (PNRA), are located near the CGT.

Spatiotemporal variations of fast ice dynamics in this region have been a major issue for the logistics of the research stations. Fast ice has

\* Corresponding author.

E-mail address: [hoonyol@kangwon.ac.kr](mailto:hoonyol@kangwon.ac.kr) (H. Lee).

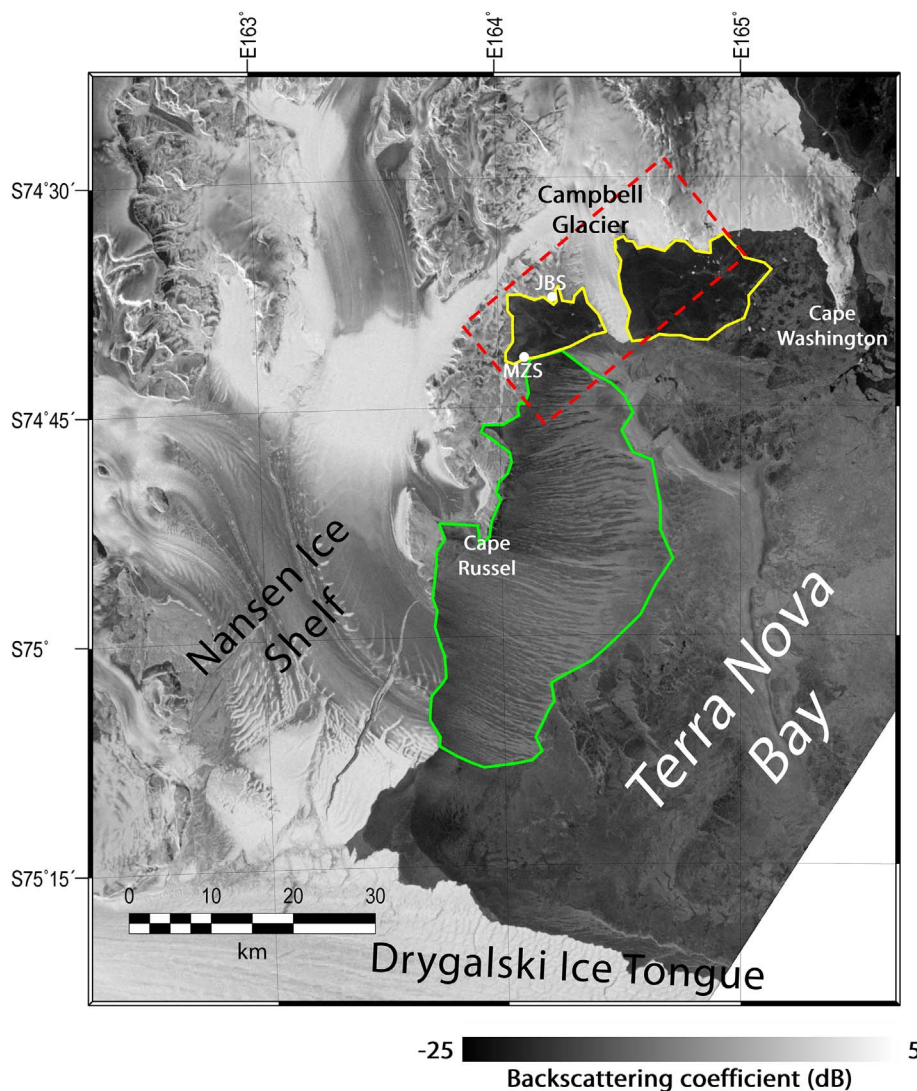


Fig. 1. Sentinel-1 SAR image over the Terra Nova Bay obtained on 4 June 2015. The red box represents the study area. A green polygon and yellow polygons represent the area of Terra Nova Bay polynya and landfast sea ice under investigation. The location of Jang Bogo Station (JBS) and Mario Zucchelli Station (MZS) are presented as white dots. (For interpretation of the references to color in this figure legend, the reader is referred to the web version of this article.)

been used as a runway for airplanes and as the transport path of supplies for the research stations. Moreover, changes in fast ice area can affect the variability of the Terra Nova Bay polynya, which produces  $\sim 5.9 \times 10^{10} \text{ m}^3$  of sea ice every year. It also contributes to the formation of the Antarctic Bottom Water in the Ross Sea (Nihashi and Ohshima, 2015).

Fast ice dynamics can be investigated by analyzing the strain that indicates the deformation characteristics of the ice. Fast ice can show large deformation even though it is attached to the coastline. This is because the strain of sea ice can be influenced by stresses from various factors such as wind, current, Coriolis force, the sea surface tilt caused by the tide, and the presence of adjacent sea ice or glaciers (Wadhams, 2000).

Synthetic Aperture Radar (SAR) provides high resolution images with all-weather and day-and-night capabilities. It has been widely used for studies of sea ice, such as classification of ice types (Zakhvatkina et al., 2013; Moen et al., 2015; Ressel et al., 2015), measurement of sea ice concentration (Belchansky and Douglas, 2002; Karvonen, 2012; Han et al., 2016), and estimation of sea ice motion (Kwok et al., 2003; Thomas et al., 2008; Komarov and Barber, 2014; Lehtiranta et al., 2015).

Using the Interferometric SAR (InSAR) technique, the displacement

of sea ice can be measured with centimeter accuracy, which can provide highly accurate information regarding strain (Dammert et al., 1998; Berg et al., 2015; Han and Lee, 2017). InSAR pairs with short temporal baselines (such as one-day) are required to avoid temporal decorrelation and to measure fast ice strain under severe stress. In this case, the InSAR signals include displacements due to the impact of all the individual factors that affect the strain of fast ice.

In the TNB, the katabatic wind is strong and contributes to the extension of sea ice in the region (Bromwich, 1989; Argentini et al., 1995). However, the drag coefficient by the katabatic wind into fast ice is low owing to a smooth ice surface with few ridges. The drag coefficient by current is low for fast ice because of the absence of a keel at the ice bottom. The Coriolis force is very strong for heavy icebergs and freely moving sea ice (i.e., drift ice or pack ice), but weak for fast ice (Wadhams, 2000). No meaningful correlation has been found so far between those factors and the temporal and spatial variations of the fast ice cover in the TNB. Therefore, the ice flow of glaciers near the fast ice (i.e., the CGT) and sea surface tilt by tide are presumably the main contributors to the strain of fast ice in the region.

Stress from the CGT is cumulative with time owing to its continuous ice flow, while that from the ocean tide is oscillatory. This means that the glacial strain on fast ice can appear to be dominant in InSAR images

with a temporal baseline of a few days or a week, while tidal signals would rarely be shown in the InSAR images. Meanwhile, tidal strain of fast ice can be observed by the Double-Differential Interferometric SAR (DDInSAR) technique, which can remove the glacial strain if the flow velocity of the CGT is constant during the observation period (Rignot, 1996; Han and Lee, 2014; Han and Lee, 2015; Han and Lee, 2017). The previous works by Han and Lee (2014, 2015, 2017) used a series of one-day InSAR and DDInSAR images for CGT. They explored ice dynamics of CGT such as tidal deflection, glacier velocity and mass balance, and did not investigate strains over the fast ice near CGT. Combination of one-day, weekly InSAR and DDInSAR images can be effectively used to identify the characteristics of glacial and tidal strains of fast ice in the Antarctica, but no similar studies have conducted so far.

Few studies have attempted to investigate the strains of fast ice caused by glacial flow, the tidal tilt of the sea surface, and their annual variations. In this study, we separate the glacial and tidal strain of fast ice around the CGT from one-day InSAR images by analyzing the equi-displacement lines of fringes in the weekly InSAR and DDInSAR images. The one-day InSAR-derived glacial and tidal strain rates of the fast ice are then decomposed and compared with those derived from the weekly InSAR and DDInSAR images. Section 2 describes the study area and presents the dataset used in this study. Section 3 describes the methodology for the characterization of the glacial and tidal strain from the weekly InSAR and DDInSAR images. Section 4 presents the results and discussion, while Section 5 concludes this paper.

## 2. Study area and data

### 2.1. Study area

The TNB lies between the Drygalski Ice Tongue (75°24'S, 163°30'E) and Cape Washington (74°39'S, 165°25'E) along the coast of East Antarctica (Fig. 1). The TNB is covered with sea ice, except during the Antarctic summer. A large coastal latent heat polynya, called the TNB polynya, typically forms between the Drygalski Ice Tongue and MSZ. The width of TNB polynya can be extended to the Cape Washington (Hollands and Dierking, 2016). This plays a key role in the formation of the Antarctic Bottom Water in the Ross Sea (Nihashi and Ohshima, 2015). Fast ice forms in the eastern section of the TNB, between the TNB polynya and Cape Washington. This area showed a maximum wind speed of  $35 \text{ m s}^{-1}$ , and the annual variations in air temperature range from  $-34^\circ\text{C}$  to  $7^\circ\text{C}$ , as measured by an automatic weather system (AWS) installed at JBS during 2010–2012. The daily variation in tide height in the fast ice area is up to 60 cm (Han and Lee, 2014; Han and Lee, 2015). The Sentinel-1A C-band SAR image of Fig. 1 shows the spatial distribution of TNB polynya (green polygon) and the nearby fast ice (yellow polygons). The polynya formed between the Drygalski Ice Tongue and near the MSZ, and shows katabatic wind-blowing signals on the ocean surface. The fast ice with low backscattering due to smooth ice surface formed at the east and west of CGT. Fig. 1 clearly shows that the TNB polynya is boarded on the fast ice formed at the west of CGT.

A previous study by Han et al. (2015) showed that fast ice in this region began to appear in March, two months after the air temperature had dropped below the freezing point, and some of it survived the summer melt. Han and Lee (2015) reported that the gravitational ice flow of the CGT increased from the grounding line ( $\sim 52 \text{ cm d}^{-1}$ ) to the seaward edge of the ice ( $\sim 67 \text{ cm d}^{-1}$ ). This was measured using COSMO-SkyMed one-day InSAR pairs obtained in 2011. The direction of the flow was also found to be constant over the whole ice tongue. Ice flow velocity of the sides of the CGT was almost constant ( $63\text{--}67 \text{ cm d}^{-1}$ ), and its magnitude was similar to that of the sea surface tilt by tide ( $\sim 60 \text{ cm}$ ) (Han and Lee, 2014; Han and Lee, 2015).

### 2.2. Data

A total of 70 COSMO-SkyMed SAR images over the fast ice area around the CGT were obtained, covering the period from December 2011 to January 2012. The COSMO-SkyMed constellation is composed of four satellites equipped with X-band SAR with a center frequency of 9.6 GHz. Each COSMO-SkyMed satellite repeats the same ground track every 16 days (Bianchessi and Righini, 2008). To obtain interferometric data, all the COSMO-SkyMed satellites follow the same ground track with the same geometric conditions. In the interferometric configuration, the COSMO-SkyMed-3, -4, and -1 satellites revisit the same ground track as the COSMO-SkyMed-2 after 1 day, 4 days and 8 days, respectively (Covello et al., 2010).

All the SAR images used in this study were acquired on the same ground track by the COSMO-SkyMed-1, -2, and -3 satellites with the same geometric conditions. They have a 3-m resolution in strip-map mode, VV-polarization, and an incidence angle of  $40^\circ$  in descending orbit at around 3:45 UTC. These satellites can make InSAR pairs with temporal baselines of 1 day, 7 days, and 8 days.

The Ross\_Inv tide model (Padman et al., 2003a) was used to predict the tide height in the TNB. The load tide effect was corrected using the TOPEX/Poseidon Global Inverse Solution (TPXO) Version 6.2 (TPXO6.2) Load Tide model (Egbert and Erofeeva, 2002). The inverse barometer effect (IBE) of the predicted tide height, that is, the rise in tide height of about 1 cm for every 1 mbar drop in atmospheric pressure (Padman et al., 2003b), was corrected using the in situ atmospheric pressure data measured by an AWS installed at the JBS.

The IBE-corrected Ross\_Inv model can be used as the optimum tide model over the TNB (Han et al., 2013) because it has a very small root mean square deviation of 4.1 cm between the tide height predicted by the model and that measured by a tide gauge in the TNB. This is smaller than those produced by other tide models such as the Circum-Antarctic Tidal Simulation, Inverse Model Version 2008a (CATS2008a) (Padman et al., 2002; Padman et al., 2008), the Finite Element Solution Tide Model 2004 (FES2004) (Lyard et al., 2006), and TPXO7.1 (Egbert and Erofeeva, 2002).

## 3. Methods

A flowchart of the data processing and analysis is shown in Fig. 2. First, 20 one-day and 57 weekly (18 seven-day and 39 eight-day, respectively) interferograms were generated using the 70 COSMO-SkyMed SAR images. We used the Advanced Spaceborne Thermal Emission and Reflection Radiometer (ASTER)-derived Global Digital Elevation Model (GDEM) with a grid spacing of 30 m and a vertical accuracy of 20 m (Fujisada et al., 2005), to remove topographic fringes over terrain, while no elevation data were provided for sea ice.

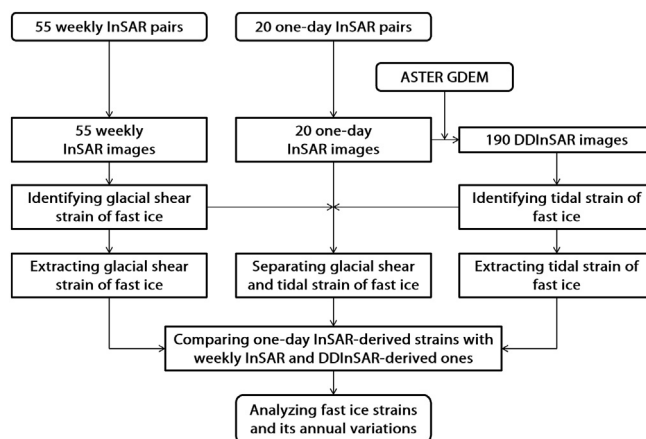


Fig. 2. Flowchart of data processing.

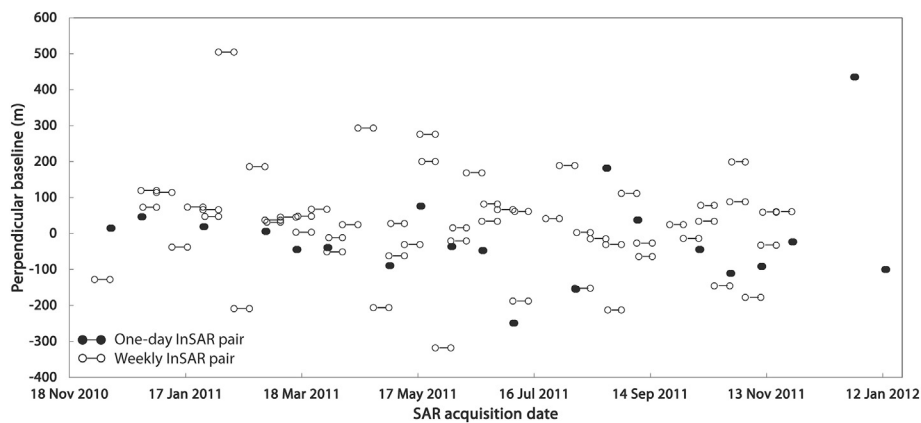


Fig. 3. Perpendicular baselines of the COSMO-SkyMed one-day and weekly InSAR pairs used in this study.

However, topographic fringes over fast ice are negligible because the perpendicular baselines of the interferograms are very short, ranging from 3 m to 504 m (Fig. 3), and the ice surface is almost flat. The following sections describe how we defined fast ice relative to open water, pack ice, or new ice. Once this had been done, we then identified the characteristics of the glacial strain by using 57 weekly InSAR images. The tidal strain was determined using 190 DDInSAR images over the fast ice. Upon identifying the fringe patterns of glacial and tidal strain, we decomposed each signal in the 20 one-day InSAR images to be compared with the results obtained from the weekly InSAR and DDInSAR images.

### 3.1. Definition of fast ice areas using InSAR coherence images

Prior to the strain analysis, fast ice has to be discriminated from open water, pack ice, and new ice (Han et al., 2015). Fig. 4a shows an example of the COSMO-SkyMed SAR image obtained on 3 June 2011, which is the inset image in Fig. 1. Pack ice contains cracks and leads, and it can be traceable by multi-temporal SAR intensity images. However, it is very difficult to define fast ice areas from SAR intensity images alone. This is because fast ice typically has a smooth surface and shows low backscattering in the SAR intensity images similar to pack ice, which also has a smooth surface. It also resembles calm open water.

Fast ice is stuck along the shoreline, but pack ice moves almost constantly, driven by currents and the wind. Therefore, the InSAR coherence of fast ice should be much higher than that of pack ice or open water. Fig. 4b shows an example of the coherence images generated from the one-day InSAR pair obtained on 3 and 4 June 2011, respectively. Sea ice around the CGT shows coherence values higher than 0.5, which can be defined as fast ice. The fast ice areas are clearly distinguishable from pack ice or open water, which have coherence values of less than 0.2. Even with the much longer temporal baseline of eight days, fast ice shows coherence values higher than 0.5 as shown in Fig. 4c.

By analyzing the interferometric coherence values, the fast ice in the study area can be divided into three regions: one is connected to the east side of the CGT (Region A, as indicated in Fig. 4b), another is connected to the west side of the CGT (Region B), and the other is near the shoreline in front of the JBS (Region C), detached from the CGT by cracks, leads, and the shoreline. The annual variations in area for fast ice, pack ice, and open water in Region B and C in 2011 were reported by Han et al. (2015) (Fig. 5). It should be noted that an increasing amount of pack ice and open sea during the early winter season from May to July 2011 was due to the expansion of the nearby polynya, which affects ocean circulation and ice bottom melting.

### 3.2. Characterization of glacial and tidal strain by the weekly InSAR and DDInSAR

Some examples of one-day InSAR images with various tidal differences predicted by the IBE-corrected Ross Inv ( $\dot{T}$ ) are shown in Fig. 6. The fast ice Regions A and B show different patterns in the equi-displacement lines of fringes according to the magnitude of  $\dot{T}$ , the tidal height difference in 24 h. This is especially the case in Region A, where fringe lines are almost parallel to the east margin of the CGT when the tidal difference is small (0.8 cm), as shown in Fig. 6a. Their direction deviates from the margin of the CGT as the absolute value of the tidal difference increases: by 8.7 cm in Fig. 6b, 14.8 cm in Fig. 6c, and 28.2 cm in Fig. 6d. Meanwhile, the equi-displacement lines of fringes in Region B are almost parallel to the west margin of the CGT when the tidal difference is low, and their direction deviates from the margin of the CGT and becomes parallel to those of Region C as the magnitude of the tidal difference increases. The fringes over fast ice Region C, which is not affected by glacial stress, follow the coastline in all one-day InSAR images, and the fringe rate would be proportional to the magnitude of  $\dot{T}$ . This is because  $\dot{T}$  is a good approximation of the time derivative of tide at a specific location (Han and Lee, 2015). As the tide is a spatio-temporal phenomenon that propagates both in space and time through the tide current, the time derivative of a tide is proportional to the spatial gradient of the tide (i.e., the ocean surface tilt), which generates tidal fringes on fast ice.

It is suggested that the fringes of glacial strain should be parallel to the glacial margin, while those of tidal strain would, instead, follow the coastlines. Therefore, fast ice in Regions A and B, which are attached to the CGT, experience glacial stress as well as tidal stress, while that in Region C is affected only by the tide. However, it is difficult to analyze the glacial and tidal strains of the fast ice regions A and B from the one-day InSAR images, as both signals have similar magnitude ( $\sim 67 \text{ cm d}^{-1}$  for glacial flow and  $\sim 60 \text{ cm}$  of tidal height) and are mixed in the images. Therefore, it is necessary to identify and separate the glacial and tidal strains in one-day InSAR by using the weekly InSAR and DDInSAR images, as outlined below.

The strain from the tide is oscillatory, while that from the flow of the CGT is cumulative with time. Therefore, glacial strain will be predominantly observed in the weekly InSAR images, while the tidal strain remains more or less the same. It is also expected that the DDInSAR operation can eliminate the glacial strain, while leaving the tidal strain. This can be done by assuming that the glacial stress is almost constant (Han and Lee, 2015) over the observation period owing to steady ice flow.

To characterize the glacial and tidal strain on the fast ice, we investigated the patterns of equi-displacement lines of fringes in the weekly InSAR and DDInSAR images. A total of 190 DDInSAR images were generated from the 20 one-day InSAR images, in which

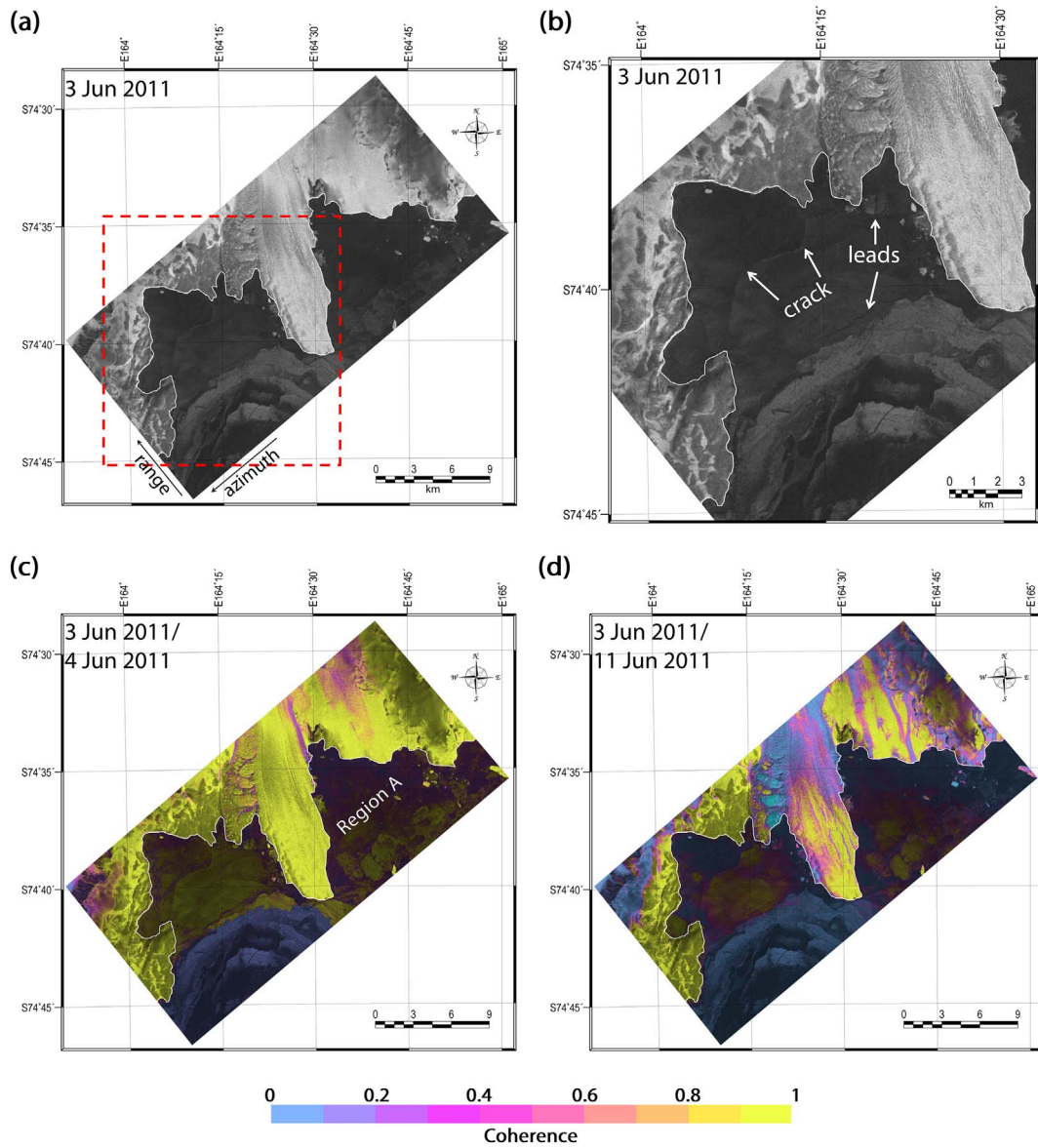


Fig. 4. (a) An example of the COSMO-SkyMed SAR image obtained on 3 June 2011. (b) Enlarged image corresponding to the red dotted box in (a). Examples of the COSMO-SkyMed (c) one-day and (d) eight-day interferometric coherence images, respectively. A white line in each image represents the coastline which was created by digitizing the coast observed in the SAR image. (For interpretation of the references to color in this figure legend, the reader is referred to the web version of this article.)

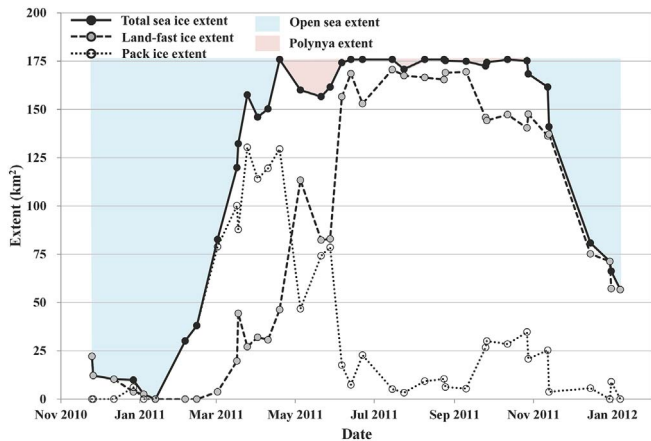


Fig. 5. The annual variation in the extent of fast ice, pack ice, the sum of the fast ice and pack ice (i.e., total sea ice extent), open sea, and polynya in Regions B and C in 2011 (Fig. 4 of Han et al., 2015).

topographic fringes over grounded ice sheets and ice shelves were removed using the ASTER GDEM. The weekly InSAR images were not used for the generation of DDInSAR images, this was because there was extreme temporal decorrelation of the fast-flowing grounded ice stream and thus it was not feasible to conduct quality control checks.

### 3.3. Decomposition of glacial and tidal strains from the one-day InSAR

After characterizing the fringe patterns and directions due to glacial and tidal strain, we decomposed and separated them from the one-day InSAR fringes, assuming that the two strain components are orthogonal to each other. In the one-day InSAR fringes, the glacial strain rate is measured along the contact line with the CGT, while the tidal strain rate is measured parallel to the coastline.

On the horizontal plane, with the  $x$ - and  $y$ -axis parallel to the coastline, and the side of the CGT, respectively (Fig. 7), the glacial and tidal strain rates ( $\dot{\epsilon}_{glac}$  and  $\dot{\epsilon}_{tide}$ ) of fast ice Regions A and B can be decomposed from the one-day InSAR signals as

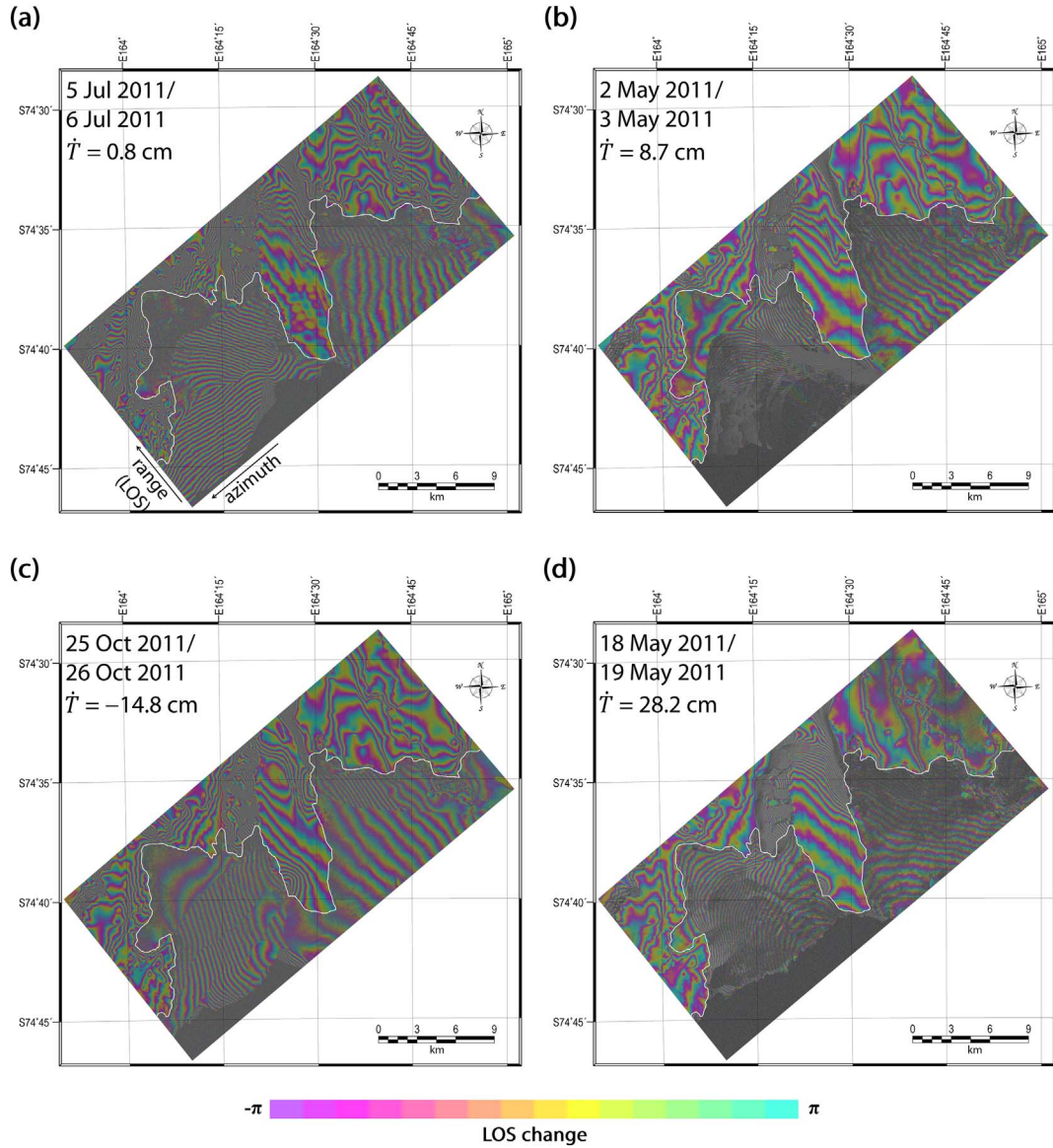


Fig. 6. Examples of COSMO-SkyMed one-day InSAR images with various tidal conditions.  $\dot{T}$  represents tidal variations during the InSAR observation. LOS in (a) means the radar line-of-sight.

$$\dot{\epsilon}_{glac} = \frac{\Delta D_{LOS} \cos \phi}{L \sin \theta} \quad [d^{-1}] \quad (1)$$

$$\dot{\epsilon}_{tide} = \frac{\Delta D_{LOS} \sin \phi}{L \cos \theta} \quad [d^{-1}] \quad (2)$$

where  $L$  is the distance between fringes orthogonal to the equi-displacement line,  $\Delta D_{LOS}$  is the displacement difference in the radar line-of-sight (LOS) direction along the  $L$ ,  $\phi$  is the angle of the propagation direction of the fringes measured clockwise from the x-axis, and  $\theta$  is the radar incidence angle. The  $\dot{\epsilon}_{tide}$  in Eq. (2) is estimated in the vertical direction to represent the vertical tidal flexure of the ice. In Region C,  $\dot{\epsilon}_{glac}$  was not considered because the ice was isolated from the CGT by cracks and leads.

$\dot{\epsilon}_{glac}$  and  $\dot{\epsilon}_{tide}$  extracted from the one-day InSAR images were compared with those derived from the weekly InSAR and DDInSAR images. This provided information on the reliability of the decomposition scheme from the one-day InSAR images, as well as utilizing all data from the one-day InSAR, weekly InSAR, and DDInSAR images.

## 4. Results and discussion

### 4.1. Glacial strain in the weekly InSAR images

Fig. 8 shows some examples of weekly InSAR images with various tidal conditions ( $\dot{T}$ ) predicted by the IBE-corrected Ross\_Inv model. Although the values of  $\dot{T}$  are different, the equi-displacement lines of fringes over fast ice Regions A and B are almost parallel to the contact line with the CGT in all the weekly InSAR images. This confirms that the dominant fringes in the weekly InSAR images are caused by the cumulative stress from a steady flow of the CGT over the week ( $\sim 469$  cm/week; Han and Lee, 2015), while the oscillating tidal strain remains the same ( $\sim 60$  cm).

Fringes in the fast ice in Regions A and B indicate that the magnitude of displacement of the ice linearly changes as distance from the CGT increases. Based on the fact that the fast ice is attached to the coastline and to the contact sides of the CGT, and that the flow direction of the CGT is parallel to the contact line between the fast ice and the CGT, stress from the flow of the CGT acts as a shearing force on the fast ice. Thus, the fast ice in Regions A and B experiences shear displacement by glacial shear forcing, the magnitude of which decreases as

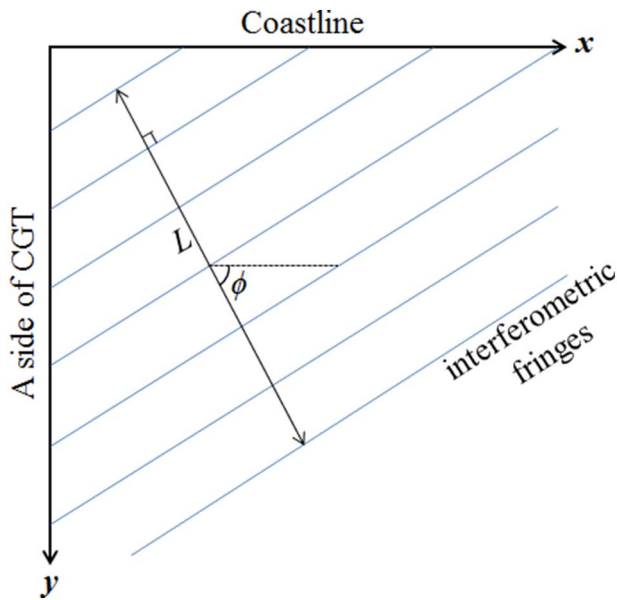


Fig. 7. A schematic for the decomposition of glacial and tidal strains from one-day InSAR signals.

distance from the CGT increases. The weekly InSAR images show that the fringes of Region C follow the shoreline owing to the tide, while stress from the CGT does not reach this region.

#### 4.2. Tidal strain in the DDInSAR images

Fast ice bends owing to sea surface tilt from the tide, and the magnitude of the tidal displacement will increase from the hinge line (i.e., the coastline) to the seaward edge of the ice (Vaughan, 1995). The fast ice in Regions A and B is in contact with the CGT; however, the CGT does not play the role of a grounding line. This is because the tide deflection ratio, defined as the ratio of the vertical tidal deflection over tide height, of the side of the CGT is almost 1 (Han and Lee, 2014). It also experiences tidal flexure with the same magnitude as the tidal height. The fast ice in Region B is attached to the seaward edge of the fast ice in Region C, and the shoreline in front of the MZS as well. The width of the shoreline near the MZS, which is in contact with Region B, is very narrow. This means that it would not function properly as a hinge line. As a whole, we expect that the tidal fringes of fast ice in Regions A and B also follow the coastline regardless of the presence of the CGT.

To verify the tidal displacement of the fast ice regions, we investigated the DDInSAR images. Some examples of the DDInSAR images with various double-differential tide heights ( $\Delta\hat{T}$ ) are shown in Fig. 9. These were predicted by the IBE-corrected Ross\_Inv model. The equi-displacement lines for the fringes over the fast ice in Region C follow the shoreline because the ice only experiences the tidal stress. In the fast ice in Regions A and B, the fringes follow the shoreline, especially in the case of large tidal variations, and are not affected by the CGT (Fig. 9a and b).

In the case of low tidal variations (Fig. 9c and d), however, the fringes follow both the shoreline and the edge of the CGT. This is because the glacial strain on the fast ice would vary slightly with time, probably because of the temporal changes in the physical properties of the fast ice such as ice thickness and elastic modulus (Hibler III, 1979; Hunke and Dukowicz, 1997; König Beatty and Holland, 2010). Seasonal variations in the glacial strain rate in those regions, together with the more detailed analysis of their tidal responses, will be discussed in the following three sections.

#### 4.3. Region A: fast ice attached to the east of the CGT

The black points in Fig. 10a show the temporal variation of the glacial shear strain rate ( $\dot{\epsilon}_{glac}$ ) of the fast ice attached to the east of the CGT (Region A), decomposed from the one-day InSAR images by Eq. (1). The solid line is a regression curve of this data. The  $\dot{\epsilon}_{glac}$  estimated from the weekly InSAR images and its temporal variation are shown as white points and the dotted curve in Fig. 10a. In each fast ice region, the glacial shear and tidal strain rates were calculated once along  $L$  at an area where the fringes are well observed from the one-day, weekly and DDInSAR images. It can represent the region because the  $L$  was spatially constant. The weekly InSAR-derived  $\dot{\epsilon}_{glac}$  are very consistent with the one-day InSAR-derived data from throughout the year. This comparison verifies that the proposed decomposition of glacial strain from the one-day InSAR images is reliable. This decomposition method would be especially useful to investigate the glacial strain of the fast ice, when temporal decorrelation of the ice is too severe to generate long-term InSAR data.

The strain rate decreased from May ( $3.49 \times 10^{-5} \text{ d}^{-1}$ ) to late August ( $1.90 \times 10^{-5} \text{ d}^{-1}$ ), and then stabilized until the end of December ( $1.85 \times 10^{-5} \text{ d}^{-1}$ ). This shows that the shear deformation of the fast ice in this region decreased from the time of freeze onset to late August. This is likely due to increased resistivity from ice thickening. The ice maintained its thickness and strength until December. It is worth noting that seasonal variations in ice thickness information of fast ice can be inferred by observing the change of the glacial strain rates from a series of InSAR observations where in situ data collection is extremely limited.

The tidal strain rate ( $\dot{\epsilon}_{tide}$ ) of the fast ice in Region A was computed from the one-day InSAR images using Eq. (2). It was compared with  $\hat{T}$  during the InSAR observations predicted by the IBE-corrected Ross\_Inv tide model (black points in Fig. 10b). The linear regression between the one-day InSAR-derived  $\dot{\epsilon}_{tide}$  and  $\hat{T}$  shows a very high  $R^2$  value of 0.939, with a slope of  $4.870 \times 10^{-7}$  (black regression line in Fig. 10b). The high  $R^2$  value shows that the  $\dot{\epsilon}_{tide}$  of the fast ice is hardly influenced by the seasonal changes in the physical properties of the ice, unlike the  $\dot{\epsilon}_{glac}$ .

The tidal strain rate ( $\dot{\epsilon}_{tide}$ ) was estimated from the DDInSAR images and compared with  $\Delta\hat{T}$  during the observations predicted by the IBE-corrected Ross\_Inv model. These results are shown as white points in Fig. 10b. In total, 15 DDInSAR images were generated out of the one-day InSAR pairs obtained from late August to November, when glacial strain is stabilized so that the glacial strain would be cancelled out during the double-differencing operation (Rignot, 1996; Han and Lee, 2014; Han and Lee, 2015). The slope of the linear regression between the DDInSAR-derived  $\dot{\epsilon}_{tide}$  and  $\Delta\hat{T}$  (the dotted regression line in Fig. 10b) is  $4.38 \times 10^{-7}$ . This is slightly different from that estimated by the decomposed tidal strain from the one-day InSAR images ( $4.87 \times 10^{-7}$ ). The  $R^2$  value of the linear regression between the DDInSAR-derived  $\dot{\epsilon}_{tide}$  and  $\Delta\hat{T}$  is 0.705, which is lower than that between the one-day InSAR-derived  $\dot{\epsilon}_{tide}$  and  $\hat{T}$  (0.939). This is partially because the DDInSAR signals still contained some residuals of  $\dot{\epsilon}_{glac}$  during the observations, as shown in Fig. 10a. The very high  $R^2$  value of the linear regression between the one-day InSAR-derived  $\dot{\epsilon}_{tide}$  and tide variations prove that the decomposition method is very reliable in this region.

#### 4.4. Region B: fast ice attached to the west of the CGT

The glacial strain rate ( $\dot{\epsilon}_{glac}$ ) of the fast ice connected to the west of the CGT (Region B) was also decomposed from the one-day InSAR images, as shown by the black points and solid regression curve in Fig. 11a. The temporal variation of  $\dot{\epsilon}_{glac}$  derived from the weekly InSAR images (the white points and dotted line in Fig. 11a) also shows that the fast ice in Region B experienced increasing shear deformation until early September. Thereafter, it decreased, showing very small

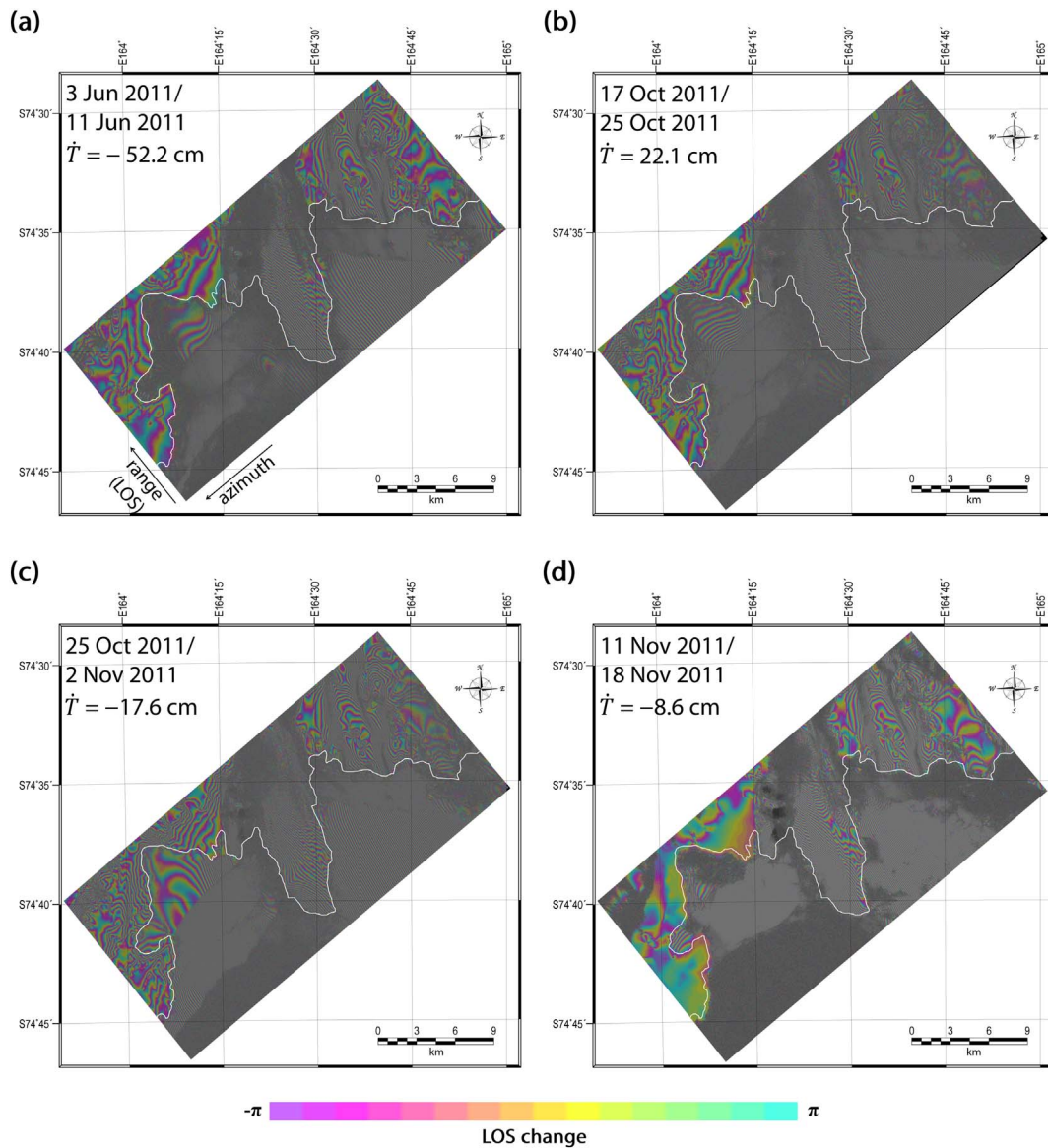


Fig. 8. Examples of COSMO-SkyMed weekly InSAR images with various tidal conditions.  $\dot{T}$  represents tidal variations during the InSAR observation.

deviations from those derived by the one-day InSAR images. This also confirms that  $\dot{\epsilon}_{glac}$  of the fast ice decomposed from the one-day InSAR images is also reasonable in Region B.

The temporal variation of  $\dot{\epsilon}_{glac}$  for the fast ice in Region B has quite a different seasonal trend from that in Region A. The rate started with a similar value ( $3.35 \times 10^{-5} \text{ d}^{-1}$ ) to Region A in May. As the winter deepened,  $\dot{\epsilon}_{glac}$  sharply increased until July, and reached a local maximum in September ( $5.66 \times 10^{-5} \text{ d}^{-1}$ ). It then decreased until December ( $3.78 \times 10^{-5} \text{ d}^{-1}$ ). In terms of ice thickness, this trend can be interpreted as a rapid ice thinning from May to July, stabilization from July to September, and ice thickening thereafter. One possible explanation for this anomaly is that the fast ice in Region B shares a boundary with a large polynya in the TNB (Ciappa and Pietranera, 2013; Hollands and Dierking, 2016). An increased ocean circulation near the fast ice edge in the polynya expansion period would have caused bottom melting, and thus ice thinning, of the fast ice in the early winter (Langhorne et al., 2001; Massom and Stammerjohn, 2010; Rusciano et al., 2013). As the winter deepened, the effect of the polynya on the fast ice would have decreased because pack ice formed at the seaward edge of the fast ice. This explanation coincides with Fig. 5 showing that a polynya began to appear in April, expanded to its

maximum of 20 km<sup>2</sup> in May, and disappeared completely in June in the study area. The continuous decrease of the glacial strain during December–January period is not clear due to the lack of data point but might be caused by the on-going thickening of fast ice owing to the reduced polynya activity and still low temperature. Another possible explanation to it could be that the shearing of fast ice due to glacial stresses was prevented by the surrounding pack ice. However, the relationship between polynya, pack ice and glacial strain in the ice-melting season needs further investigation.

The tidal strain rate ( $\dot{\epsilon}_{tide}$ ) of this region was decomposed from the one-day InSAR images using Eq. (2). Fig. 11b shows a linear regression between  $\dot{\epsilon}_{tide}$  and  $\dot{T}$  during the InSAR observations predicted by the IBE-corrected Ross\_Inv model (the black points and solid regression line in Fig. 11b). The values of  $\dot{\epsilon}_{tide}$  is highly correlated with the tidal variations, showing an R<sup>2</sup> value of 0.80. This represents the fact that  $\dot{\epsilon}_{tide}$  of the fast ice in Region B was hardly affected by the seasonal changes in the physical properties of the ice, which fits the pattern seen for the fast ice in Region A.

The slope of the linear regression was estimated to be  $1.27 \times 10^{-6}$ , which is about 2.6 times greater than that from the fast ice in Region A ( $0.49 \times 10^{-6}$ ). The greater tidal response of Region B compared with

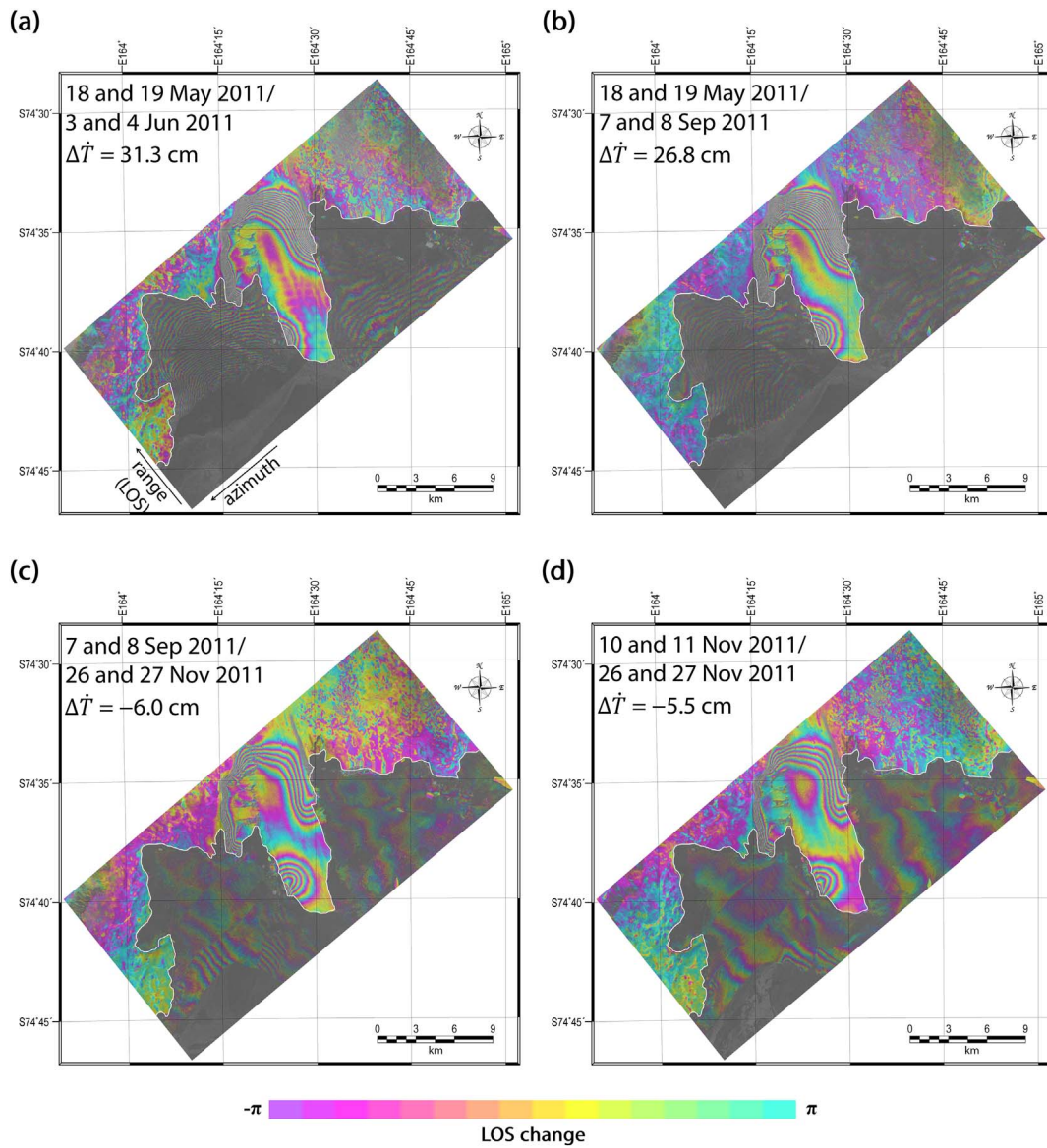


Fig. 9. Examples of COSMO-SkyMed DDInSAR images with various tidal conditions.  $\Delta\dot{T}$  represents the tidal variation during the DDInSAR observation.

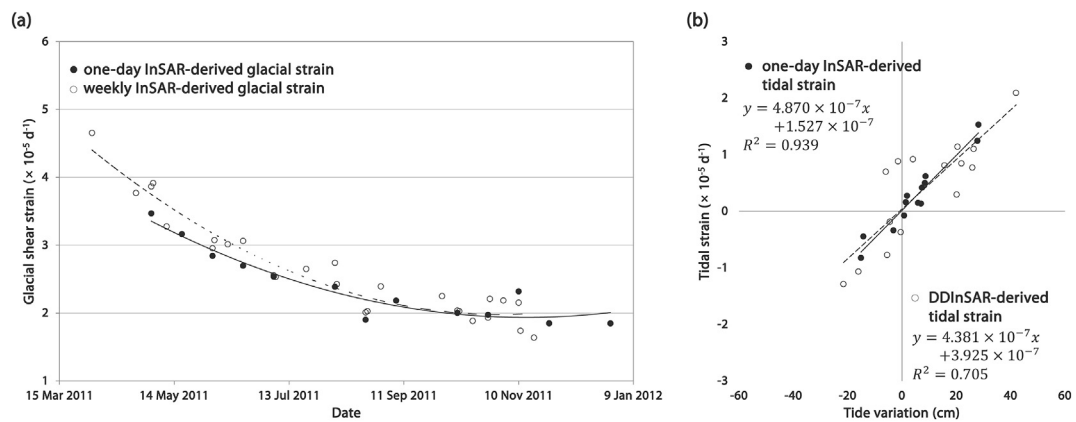


Fig. 10. (a) Glacial shear strain of the fast ice connected to the east of the CGT (fast ice Region A). The one-day InSAR-derived glacial strain and its temporal variation pattern are represented as black points and the solid line, respectively. The weekly InSAR-derived data are represented as white points and with a dotted line, respectively. (b) Linear regression between tidal strain of the fast ice connected to the east of the CGT, and tidal variation predicted by the IBE-corrected Ross\_Inv model. The black points and solid regression line correspond to the one-day InSAR-derived tidal strain, while the white points and dotted regression line correspond to the DDInSAR-derived ones.

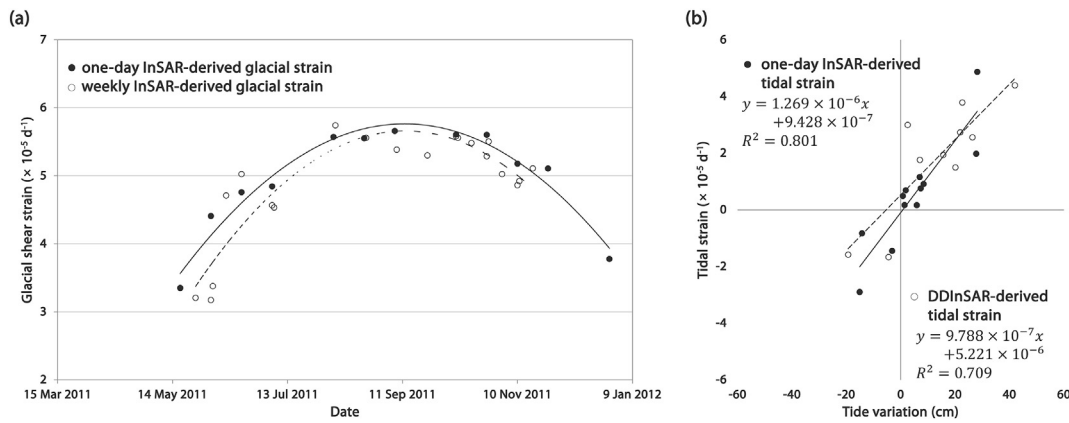


Fig. 11. (a) Glacial shear strain of the fast ice connected to the west of the CGT (fast ice Region B). The one-day InSAR-derived glacial strain and its temporal variation pattern are represented by the black points and a solid line, respectively, while the weekly-InSAR-derived ones are represented by the white points and a dotted line, respectively. (b) Linear regression between the tidal strain of the fast ice connected to the west of the CGT and tide variation predicted by the IBE-corrected Ross\_Inv model. The black points and the solid regression line correspond to the one-day InSAR-derived tidal strain, while the white points and the dotted regression line correspond to the DDInSAR-derived ones.

Region A could be caused by thinner ice in Region B due to the nearby polynya. A stronger local tidal current (or ocean surface tilt) in Region B is also suspected as it is surrounded by the TNB and CGT. More detailed observations of the ice thickness and local tide currents are necessary to clarify this issue.

A total of 10 DDInSAR images were generated from the one-day InSAR pairs obtained during August to October, when the temporal variation of glacial strain rate is at its minimum (less than  $9 \times 10^{-7} \text{ d}^{-1}$ ) throughout the observation period. A linear regression between the DDInSAR-derived  $\dot{\epsilon}_{tide}$  and  $\Delta\dot{T}$  during the observations predicted by the IBE-corrected Ross\_Inv model is shown as white points with a dotted regression line in Fig. 11b. The slope and  $R^2$  of the linear regression were estimated to be  $9.788 \times 10^{-7}$  and 0.709, respectively. These values are lower than those of the one-day InSAR-derived  $\dot{\epsilon}_{tide}$  and  $\dot{T}$ , possibly due to the remaining glacial strain rates during the DDInSAR operation.

4.5. Region C: fast ice attached to the coast and isolated from the CGT

The equi-displacement lines of fringes in the one-day and weekly InSAR and DDInSAR images show that the fast ice attached to the shoreline in front of the JBS (Region C) is mainly affected by sea surface tilt due to tide current. Fig. 12 shows the linear regressions between the one-day InSAR, weekly InSAR, and DDInSAR-derived  $\dot{\epsilon}_{tide}$ , along with tidal variations during each observation as predicted by the IBE-corrected Ross\_Inv model. All regressions show a similar slope ( $1.39 \times 10^{-6}$ ,  $1.35 \times 10^{-6}$ , and  $1.4 \times 10^{-6}$  from the one-day, weekly, and DDInSAR, respectively) with high  $R^2$  values (0.91, 0.87, and 0.92

from the one-day, weekly, and DDInSAR, respectively). This confirms that the strain of the fast ice in Region C is only affected by tidal stress, and  $\dot{\epsilon}_{tide}$  in the region is hardly affected by the seasonal changes in physical properties of the ice. The values of the slope of the regressions between  $\dot{\epsilon}_{tide}$  and the tidal variations for the fast ice, which represent the strain of the ice responding to the sea surface tilt, are similar to those for the ice connected to the west of the CGT (Region B). This result sounds plausible as they are located close to each other.

5. Conclusion

The glacial shear strain and tidal strain of fast ice in the TNB, East Antarctica, were separated from a series of COSMO-SkyMed one-day InSAR pairs by identifying the characteristics of the strains from weekly InSAR and DDInSAR images. Their seasonal variations were investigated. Areas of fast ice were discriminated from areas of pack ice and open water by analyzing interferometric coherence values, which showed annual variations of fast ice and the seasonal growth of the nearby polynya. The weekly InSAR images predominantly showed glacial shear strain of the fast ice with the fringes parallel to the sides of the CGT. Conversely, the DDInSAR images showed tidal deformation of the ice, with the fringes parallel to the coastline. The strains were separated from the one-day InSAR images by decomposing the fringe patterns based on their unique characteristics, which were consistent with those estimated from the weekly InSAR and DDInSAR images.

Fast ice attached to the east of the CGT (Region A) showed glacial shear strain due to the constant flow of the CGT. The magnitude of this strain decreased during the ice thickening period from May to August

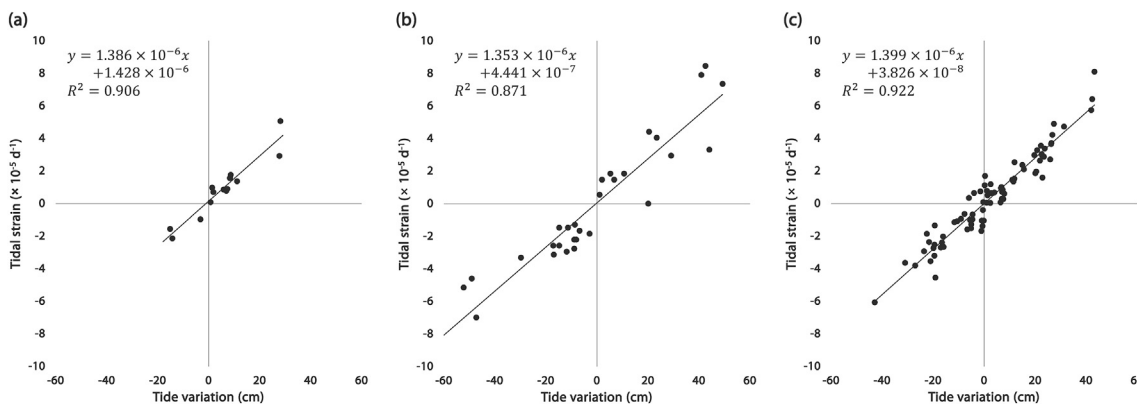


Fig. 12. Linear regressions between tide variation predicted by the IBE-corrected Ross\_Inv model and (a) one-day InSAR, (b) weekly InSAR, and (c) DDInSAR-derived tidal strain of the fast ice near of Jang Bogo Station, isolated from the CGT (fast ice in Region C).

and then stabilized until December. The fast ice to the west of the CGT (Region B) showed glacial strain increasing from May to July, possibly due to the thinning of the ice by bottom melting, caused by the increased ocean circulation during the nearby polynya extension period. It then decreased until December owing to the decreased influence of the polynya. The fast ice near the Jang Bogo Station (Region C), isolated from the CGT by cracks and leads, only showed tidal strain. Tidal strain of the fast ice was strongly correlated with the magnitude of tide variations in all regions. The stronger tidal response in Regions B and C suggested that ice is thinner there than in Region A.

The above results show that weekly InSAR (or InSAR with a temporal baseline longer than one day) can successfully highlight steadily accumulating glacial strain over oscillatory tidal strain. DDInSAR is useful to extract tidal strain by removing steady glacial strain. It is also suggested that the glacial and tidal strains decomposed from the one-day InSAR images are valid, and that the decomposition method developed in this research is a useful technique. This is especially true when InSAR with a longer temporal baseline, or DDInSAR operations are not a feasible option owing to severe temporal decorrelation or a limited dataset.

### Acknowledgement

This research was supported by the National Research Foundation of Korea [Grant Number: NRF-2016R1D1A1A09916630], the Korea Polar Research Institute (KOPRI) Grant PE17340 and PE17120, and the Korea Ministry of Environment as "The GAIA project".

### References

- Argentini, S., Del Buono, P., Della Vedova, A.M., Mastrantonio, G., 1995. A statistical analysis of wind in Terra Nova Bay, Antarctica, for the austral summers 1988 and 1989. *Atmos. Res.* 39 (1), 145–156.
- Belchinsky, G.I., Douglas, D.C., 2002. Seasonal comparisons of sea ice concentration estimates derived from SSM/I, OKEAN, and RADARSAT data. *Remote Sens. Environ.* 81 (1), 67–81.
- Berg, A., Dammert, P., Eriksson, L.E.B., 2015. X-band interferometric SAR observations of Baltic fast ice. *IEEE Trans. Geosci. Remote Sens.* 53 (3), 1248–1256.
- Bianchessi, N., Righini, G., 2008. Planning and scheduling algorithms for the COSMO-SkyMed constellation. *Aerosp. Sci. Technol.* 12 (7), 535–544.
- Bromwich, D.H., 1989. An extraordinary katabatic wind regime at Terra Nova Bay, Antarctica. *Mon. Weather Rev.* 117 (3), 688–695.
- Ciappa, A., Pietranera, L., 2013. High resolution observations of the Terra Nova Bay polynya using COSMO-SkyMed X-SAR and other satellite imagery. *J. Mar. Syst.* 113–114, 42–51.
- Covello, F., Battazza, F., Coletta, A., Lopinto, E., Fiorentino, C., Pietranera, L., Valentini, G., Zoffoli, S., 2010. COSMO-SkyMed an existing opportunity for observing the Earth. *J. Geodyn.* 49 (3), 171–180.
- Dammert, P.B.G., Lepparanta, M., Askne, J., 1998. SAR interferometry over Baltic Sea ice. *Int. J. Remote Sens.* 19 (16), 3019–3037.
- Egbert, G.D., Erofeeva, S.Y., 2002. Efficient inverse modeling of barotropic ocean tides. *J. Atmos. Ocean. Technol.* 19 (2), 183–204.
- Fraser, A.D., Massom, R.A., Michael, K.J., Galton-Fenzi, B.K., Lieser, J.L., 2012. East Antarctic landfast sea ice distribution and variability, 2000–08. *J. Clim.* 25 (4), 1137–1156.
- Fujisada, H., Bailey, G.B., Kelly, G.G., Hara, S., Abrams, M.J., 2005. ASTER DEM performance. *IEEE Trans. Geosci. Remote Sens.* 43 (12), 2707–2714.
- Giles, A.B., Massom, R.A., Lytle, V.I., 2008. Fast-ice distribution in East Antarctica during 1997 and 1999 determined using RADARSAT data. *J. Geophys. Res.* 113 (C02S14). <http://dx.doi.org/10.1029/2007JC004139>.
- Han, H., Lee, H., 2014. Tide deflection of Campbell Glacier Tongue, Antarctica, analyzed by double-differential SAR interferometry and finite element method. *Remote Sens. Environ.* 141, 201–213.
- Han, H., Lee, H., 2015. Tide-corrected flow velocity and mass balance of Campbell Glacier Tongue, East Antarctica, derived from interferometric SAR. *Remote Sens. Environ.* 160, 180–192.
- Han, H., Lee, H., 2017. Surface strain rates and crevassing of Campbell Glacier Tongue in East Antarctica analysed by tide-corrected DInSAR. *Remote Sens. Lett.* 8 (4), 330–339.
- Han, H., Lee, J., Lee, H., 2013. Accuracy assessment of tide models in Terra Nova Bay, East Antarctica, for glaciological studies of DDInSAR technique. *Korean J. Remote Sens.* 29 (4), 375–387.
- Han, H., Kim, Y., Jin, H., Lee, H., 2015. Analysis of annual variability of landfast sea ice near Jangbogo Antarctic Station using InSAR coherence images. *Korean J. Remote Sens.* 31 (6), 501–512.
- Han, H., Im, J., Kim, M., Sim, S., Kim, J., Kim, D.J., Kang, S.H., 2016. Retrieval of melt ponds on Arctic multiyear sea ice in summer from TerraSAR-X dual-polarization data using machine learning approaches: a case study in the Chukchi Sea with mid-incidence angle data. *Remote Sens.* 8 (1), 57.
- Hibler III, W.D., 1979. A dynamic thermodynamic sea ice model. *J. Phys. Oceanogr.* 9 (4), 815–846.
- Hollands, T., Dierking, W., 2016. Dynamics of the Terra Nova Bay Polynya: the potential of multi-sensor satellite observations. *Remote Sens. Environ.* 187, 30–48.
- Hunke, E.C., Dukowicz, J.K., 1997. An elastic-viscous-plastic model for sea ice dynamics. *J. Phys. Oceanogr.* 27 (9), 1849–1867.
- Karvonen, J., 2012. Baltic sea ice concentration estimation based on C-band HH-polarized SAR data. *IEEE J. Sel. Topics Appl. Earth Observ. Remote Sens.* 5 (6), 1874–1884.
- Kim, M., Im, J., Han, H., Kim, J., Lee, S., Shin, M., Kim, H., 2015. Landfast sea ice monitoring using multisensory fusion in the Antarctic. *GISci. Remote Sens.* 52 (2), 239–256.
- Komarov, A.S., Barber, D.G., 2014. Sea ice motion tracking from sequential dual-polarization RADARSAT-2 images. *IEEE Trans. Geosci. Remote Sens.* 52 (1), 121–136.
- König Beatty, C., Holland, D.M., 2010. Modeling landfast sea ice by adding tensile strength. *J. Phys. Oceanogr.* 40 (1), 185–198.
- Kwok, R., Cunningham, G.F., Hibler, W.D., 2003. Sub-daily sea ice motion and deformation from RADARSAT observations. *Geophys. Res. Lett.* 30 (23), 2218. <http://dx.doi.org/10.1029/2003GL018723>.
- Langhorne, P.J., Squire, V.A., Fox, C., Haskell, T.G., 2001. Lifetime estimation for a landfast ice sheet subjected to ocean swell. *Ann. Glaciol.* 33, 333–338.
- Lehtiranta, J., Siiriä, S., Karvonen, J., 2015. Comparing C-and L-band SAR images for sea ice motion estimation. *Cryosphere* 9 (1), 357–366.
- Lyard, F., Lefevre, F., Letellier, T., Francis, O., 2006. Modelling the global ocean tides: modern insights from FES2004. *Ocean Dyn.* 56, 394–415.
- Massom, R.A., Stammerjohn, S.E., 2010. Antarctic sea ice change and variability — physical and ecological implications. *Pol. Sci.* 4, 149–186.
- Massom, R.A., Hill, K.L., Lytle, V.I., Worby, A.P., Paget, M.J., Allison, I., 2001. Effects of regional fast-ice and iceberg distributions on the behaviour of the Mertz Glacier polynya, East Antarctica. *Ann. Glaciol.* 33, 391–398.
- Moen, M.A., Anfinsen, S.N., Doulgeris, A.P., Renner, A.H.H., Gerland, S., 2015. Assessing polarimetric SAR sea-ice classifications using consecutive day images. *Ann. Glaciol.* 56, 285–294.
- Nihashi, S., Oshima, K.I., 2015. Circumpolar mapping of Antarctic coastal polynyas and landfast sea ice: relationship and variability. *J. Clim.* 28 (9), 3650–3670.
- Padman, L., Fricker, H.A., Coleman, R., Howard, S., Erofeeva, L., 2002. A new tide model for the Antarctic ice shelves and seas. *Ann. Glaciol.* 34 (1), 247–254.
- Padman, L., Erofeeva, S., Joughin, I., 2003a. Tides of the Ross Sea and Ross Ice Shelf cavity. *Antarct. Sci.* 15 (1), 31–40.
- Padman, L., King, M., Goring, D., Corr, H., Coleman, R., 2003b. Ice-shelf elevation changes due to atmospheric pressure variations. *J. Glaciol.* 49 (167), 521–526.
- Padman, L., Erofeeva, S.Y., Fricker, H.A., 2008. Improving Antarctic tide models by assimilation of ICESat laser altimetry over ice shelves. *Geophys. Res. Lett.* 35, L22504. <http://dx.doi.org/10.1029/2008GL035592>.
- Ressel, R., Frost, A., Lehner, S., 2015. A neural network-based classification for sea ice types on X-band SAR images. *IEEE J. Sel. Topics Appl. Earth Observ. Remote Sens.* 8 (7), 3672–3680.
- Rignot, E., 1996. Tidal motion, ice velocity and melt rate of Petermann Gletscher, Greenland, measured from radar interferometry. *J. Glaciol.* 42 (142), 476–485.
- Rusciano, E., Budillon, G., Fusco, G., Spezie, G., 2013. Evidence of atmosphere–sea ice–ocean coupling in the Terra Nova Bay polynya (Ross Sea—Antarctica). *Cont. Shelf Res.* 61–62, 112–124.
- Thomas, M., Geiger, C.A., Kambhamettu, C., 2008. High resolution (400 m) motion characterization of sea ice using ERS-1 SAR imagery. *Cold Reg. Sci. Technol.* 52 (2), 207–223.
- Trevena, A.J., Jones, G.B., Wright, S.W., Van den Enden, R.L., 2003. Profiles of dimethylsulphoniopropionate (DMSP), algal pigments, nutrients, and salinity in the fast ice of Prydz Bay, Antarctica. *J. Geophys. Res.* 108 (C5), 3145. <http://dx.doi.org/10.1029/2002JC001369>.
- Vaughan, D.G., 1995. Tidal flexure at ice shelf margins. *J. Geophys. Res.* 100 (B4), 6213–6224. <http://dx.doi.org/10.1029/94JB02467>.
- Wadhams, P., 2000. *Ice in the Ocean*. Gordon and Breach Science Publisher, London.
- Zakhvatkina, N.Y., Alexandrov, V.Y., Johannessen, O.M., Sandven, S., Frolov, I.Y., 2013. Classification of sea ice types in ENVISAT synthetic aperture radar images. *IEEE Trans. Geosci. Remote Sens.* 51 (5), 2587–2600.